Three-Dimensional Millimeter-Wave Imaging for Concealed Weapon Detection

David M. Sheen, Douglas L. McMakin, and Thomas E. Hall

***Abstract*—Millimeter-wave imaging techniques and systems have been developed at the Pacific Northwest National Laboratory (PNNL), Richland, WA, for the detection of concealed weapons and contraband at airports and other secure locations. These techniques were derived from microwave holography techniques that utilize phase and amplitude information recorded over a two-dimensional aperture to reconstruct a focused image of the target. Millimeter-wave imaging is well suited for the detection of concealed weapons or other contraband carried on personnel since millimeter-waves are nonionizing, readily penetrate common clothing material, and are reflected from the human body and any concealed items. In this paper, a wide-bandwidth three-dimensional holographic microwave imaging technique is described. Practical weapon detection systems for airport or other high-throughput applications require high-speed scanning on the order of 3 to 10 s. To achieve this goal, a prototype imaging system utilizing a 27–33 GHz linear sequentially switched array and a high-speed linear scanner has been developed and tested. This system is described in detail along with numerous imaging results.**

***Index Terms*—Fourier optics, microwave holography, millimeter-wave imaging, surveillance, three-dimensional imaging, weapon detection.**

I. Introduction and Background

IN RESPONSE to an increasing threat of terrorism, personnel surveillance at security checkpoints, such as airports, is becoming increasingly important. Conventional systems in place at high-security checkpoints include metal detectors for personnel and X-ray systems for hand-carried items. These systems have been very effective, but have a number of shortcomings that will need to be addressed in future systems. Metal detectors can only detect metal targets, such as ordinary handguns and knives. The effectiveness of these detectors can vary depending on the quantity, orientation, and type of metal. Furthermore, no discrimination is possible between simple innocuous items, such as glasses, belt buckles, keys, etc., and actual threats. This leads to a rather high number of nuisance alarms. Modern threats include plastic or ceramic handguns and knives, as well as extremely dangerous items such as "plastic" and liquid explosives. These items cannot be detected with metal detectors.

A fundamentally different security measure is required to handle these threats. One type of system that addresses these concerns is an imaging system, which can penetrate clothing barriers to image items concealed by common clothing. This can be accomplished using X-ray imaging systems, and by recently developed millimeter-wave imaging systems [1], [2]. X-ray systems are potentially effective for this purpose. However, the perceived adverse health effects of X-ray exposure may hamper the public acceptance of these systems. Millimeter waves are high-frequency electromagnetic waves usually defined to be within the 30–300-GHz frequency band. The techniques and systems discussed here could operate at lower microwave frequency bands as well. Millimeter-wave systems are nonionizing and, therefore, pose no known health hazard at moderate power levels. Millimeter-wave imaging systems are capable of penetrating common clothing barriers to form an image of a person as well as any concealed items. Millimeter-wave systems can be very high resolution due to the relatively short wavelength (1–10 mm).

The current state-of-the-art in millimeter-wave imaging systems includes two fundamentally different techniques. The first technique uses a focal-plane two-dimensional (2-D) array of millimeter-wave detectors placed behind a large lens [2], [3]. This system can detect either passive energy emitted by the target or can use active millimeter-wave illuminators. Advantages of this technique include: 1) possible real-time operation; 2) relative compactness; and 3) operation analogous to an optical camera. Disadvantages include: 1) relatively low resolution due to the high optical F-number of a practical configuration; 2) small aperture (lens size is limited by practical constraints); 3) limited field of view; and 4) high cost for the 2-D array. The second technique uses a holographic linear array of sequentially switched transmitter receivers scanned quickly over a large aperture to actively illuminate the target [1]. This system operates at a single frequency, and is coherent, which means the phase of the returned signal is recorded, as well as the amplitude. The coherent data can be mathematically reconstructed in a computer to form a focused image of the target without the need for a lens. Advantages of this technique include: 1) near real-time operation; 2) high-resolution; 3) computer reconstruction allows focusing at any *single* depth; and 4) large aperture (full-body field of view). The primary disadvantage of this system/technique is that the close-range large-aperture operation causes the depth of focus to be very short. Therefore, the image of a target with significant depth, such as the human body, cannot be reconstructed in complete focus.

This paper details a significant extension of the holographic-imaging system from single-frequency operation to wide-band (many frequencies) operation. Rather than simply allowing the formation of 2-D images reconstructed at a variety of frequencies, wide-band imaging allows the formation of a fully focused three-dimensional (3-D) image from data gathered over a 2-D

Manuscript received November 2, 2000; revised January 18, 2001. This work was supported by the Federal Aviation Administration Technical Center.

The authors are with Battelle, Pacific Northwest National Laboratory, Richland, WA 99352 USA (e-mail: david.sheen@pnl.gov).

Publisher Item Identifier S 0018-9480(01)07583-4.

aperture. This advancement completely overcomes the focusing limitation present in the narrow-band system. A novel image-reconstruction computer algorithm was developed to allow efficient volumetric (i.e., 3-D) image reconstruction.

The imaging techniques developed in this paper were originally derived from microwave holography techniques [4], [5]. Microwave holography is very similar to acoustic holography [6], [7] and both techniques are long-wavelength implementations of the original optical holography techniques developed by Gabor *et al.* [8], [9]. All three forms of holographic imaging operate by sampling the amplitude and phase of a wavefront scattered from a target object. The sampled wavefront is then "reconstructed" either optically or by using Fourier-optics-based computer image-reconstruction algorithms. Acoustic and microwave holography are well suited to digital computer image reconstruction since the data are typically sampled by a scanned transceiver, and the relatively long wavelength allows for reasonable data size.

Millimeter-wave holographic imaging for concealed weapon detection was originally proposed by Farhat and Guard [10]. Their imaging technique utilized a stationary source and a scanned receiver system that employed optical (film-based) reconstruction. This technique was dramatically improved by Collins *et al.* [1] by utilizing a scanned transmitter receiver and digital reconstruction. Scanning the source produces high-quality imagery because the target is illuminated over a broad range of angles, both vertically and horizontally, which greatly reduces shadowing due to specular reflection.

The millimeter-wave holographic-imaging technique has been extensively developed over the last several years at the Pacific Northwest National Laboratory (PNNL), Richland, WA. The original techniques developed by Collins *et al.* [1] produced high-quality imagery. However, the depth of field was very short due to the large aperture and close-range operation. This limitation has been eliminated using the algorithm discussed in [11] and in this paper.

A fully 3-D image-reconstruction algorithm is developed in this paper. This algorithm augments the work of Soumekh [12]–[14], who developed algorithms for synthetic aperture radar (SAR) imaging, primarily by extending these techniques to 3-D imaging. Relevant 2-D and 3-D image-reconstruction work has been documented by several authors [15]–[24]. The algorithms documented by Soumekh, and in this paper, are distinguished from this work because they can operate within the near field of the imaged object. All of the image-reconstruction techniques in [15]–[24] are based on the fact that data collected at a far-field point represents a sample (or slice) of the 2-D or 3-D Fourier domain of the object. The imaging technique developed in Section III does not have the far-field requirement. This is because the curved wavefronts in the near field of the object are decomposed into plane-wave components using an additional Fourier transform step.

II. Single-Frequency Holographic Image Reconstruction

Holographic imaging is a means of forming focused images of targets from coherent-wave data gathered remotely over a 2-D aperture. The target is illuminated over a planar aperture using a diverging beam coherent source such as a microwave or acoustic-wave source. The reflected or echoed signal is then recorded coherently by the receiver, digitized, and stored in the computer. The data can then be mathematically reconstructed to form a focused image of the target's reflectivity function.

The image-reconstruction algorithm derived in this section was originally developed for acoustic holography and is described by Boyer [25]. The algorithm is sometimes referred to as the backward-wave reconstruction algorithm, and is based on Fourier optics techniques documented by Goodman [26, eqs. (3–42)]. This image-reconstruction algorithm was a significant advance over the earlier digital reconstruction techniques, which used the Fresnel approximation. This approximation severely limits resolution for near-field imaging systems. The notation has been updated to reflect a more modern use of wavenumber and angular frequency variable in place of frequency and spatial frequency variables. The notation used is consistent with that used by Soumekh in [12]–[14]. Slowly varying amplitude functions are typically ignored in the derivation, as they will not have a significant effect on the reconstructed image. Proper handling of the phase determines the effectiveness of the image reconstruction.

This section details an efficient algorithm that may be used to perform this image reconstruction. This technique relies extensively on the use of Fourier transforms that may be computed very efficiently using the fast-Fourier-transform (FFT) algorithm. The reconstruction method allows for wide beamwidths and targets in the near field of the scanned aperture. No far-field approximations are made. Therefore, the only limitation on the resolution obtained is the diffraction-limited resolution imposed by the wavelength, source and receiver beamwidths, size of aperture, and distance to the target. The reconstructed image will be in focus only over a depth of field determined by the aperture size or antenna beamwidths.

Data collection is performed by scanning a transmitting source and receiver over a rectilinear planar aperture that has one or more targets within its field of view. This system is quasi-monostatic, which means the transmitting and receiving antennas are separate, but in approximately the same location and may be assumed to be coincident at the midpoint between the two antennas.

The measurement configuration is shown in Fig. 1. The source is assumed to be at position (x', y', z_0), and a general point on the target is assumed to be at position $(x, y, 0)$. The target is assumed to be characterized by a reflectivity function $f(x, y, z)$, which is simply the ratio of reflected field to incident field.

The response at the transceiver will simply be the superposition of each point on the target multiplied by the roundtrip phase to that point or

$$s(x', y') = \iint f(x, y, z) e^{-j2k\sqrt{(x-x')^2+(y-y')^2+z_0^2}}\, dx\, dy \tag{1}$$

where the target is assumed to be flat and parallel to the scan plane, i.e., at constant z. The wavenumber is denoted by $k = \omega/c$, where ω is the temporal angular frequency and c is the

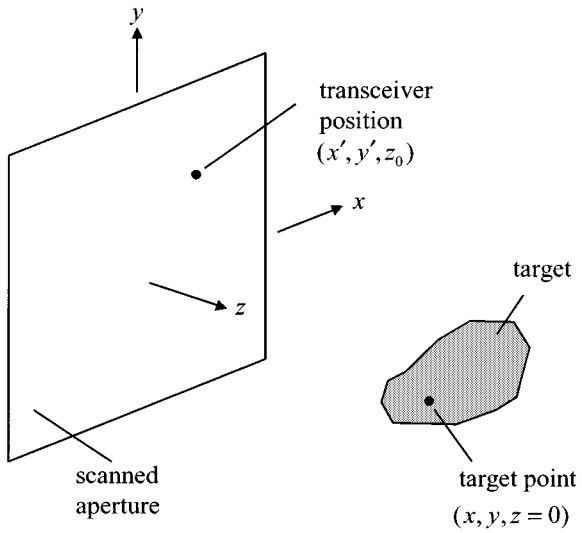

Fig. 1. Holographic imaging system configuration.

speed of light. The amplitude decay with range is not considered since it will have little impact on focusing the image. The exponential term in (1) represents a spherical wave emanating from (x', y'), which can be decomposed into a superposition of plane-wave components

$$e^{-j2k\sqrt{(x-x')^2+(y-y')^2+z^2}} = \iint e^{jk'_x(x'-x)+jk'_y(y'-y)+jk_z z_0}\, dk_{x'}\, dk_{y'} \quad (2)$$

where $k_{x'}$ and $k_{y'}$ are the Fourier-transform variables corresponding to x' and y', respectively. The spatial wavenumbers $k_{x'}$ and $k_{y'}$ will range from $-2k$ to $2k$ for propagating waves.

Using this relation and the 2-D Fourier transform definitions described in the Appendix

$$s(x', y') = \iint \underbrace{\left[\iint f(x, y, z_0) e^{-j(k_{x'}x+k_{y'}y)}\, dx\, dy\right]}_{2D \text{ Fourier Transform of } f(x,y,z_0)} \times e^{j(k_{x'}x'+k_{y'}y'+k_z z_0)}\, dk_{x'}\, dk_{y'}. \quad (3)$$

The distinction between the primed and unprimed coordinate systems is now dropped since the coordinate systems coincide. The 2-D Fourier-transform pair is defined by

$$F(k_x, k_y) = \mathrm{FT}_{2D}\{f(x, y)\} \quad (4)$$

where FT_{2D} indicates 2-D Fourier transformation.

Using the Fourier-transform relations

$$s(x, y) = \iint F(k_x, k_y) e^{jk_z z_0} e^{j(k_x x+k_y y)}\, dk_x\, dk_y \quad (5)$$

$$s(x, y) = \mathrm{FT}_{2D}^{-1}\left[F(k_x, k_y) e^{jk_z z_0}\right] \quad (6)$$

$$F(k_x, k_y) = \mathrm{FT}_{2D}\left[s(x, y)\right] e^{-jk_z z_0} \quad (7)$$

yields the inversion for the image

$$f(x, y) = \mathrm{FT}_{2D}^{-1}\left[\mathrm{FT}_{2D}\left[s(x, y)\right] e^{-jk_z z_0}\right]. \quad (8)$$

From the dispersion relation for electromagnetic plane waves

$$k_x^2 + k_y^2 + k_z^2 = (2k)^2 \quad (9)$$

$$k_z = \sqrt{4k^2 - k_x^2 - k_y^2}. \quad (10)$$

Thus, the reconstruction algorithm is summarized by

$$f(x, y) = \mathrm{FT}_{2D}^{-1}\left[\mathrm{FT}_{2D}[s(x, y)] e^{-j\sqrt{4k^2-k_x^2-k_y^2}\, z_0}\right]. \quad (11)$$

III. Wide-Band Holographic Image Reconstruction

Wide-band holographic imaging is a means of forming 3-D images of targets from wide-band data gathered over a 2-D aperture. The target is illuminated over a planar aperture using a wide-band diverging beam coherent source such as a microwave or acoustic-wave source. The reflected or echoed signal is then recorded coherently by the receiver, digitized, and stored in the computer. The data can then be mathematically reconstructed to form a 3-D image of the target's reflectivity function. This section details an efficient algorithm that may be used to perform this image reconstruction. This technique relies extensively on the use of Fourier transforms, which may be computed very efficiently using the FFT algorithm. The reconstruction method allows for wide relative bandwidths and allows for the targets to be near to the scanned aperture. No far-field approximations are made. Therefore, the only limitation on the resolution obtained is the diffraction-limited resolution imposed by the wavelength, source and receiver beamwidths, size of aperture, and distance to the target. This method is similar to single-frequency holography, with the extension to wide-band illumination, which allows for true 3-D high-resolution imagery from a 2-D planar aperture. The image-reconstruction technique assumes that the data represents a single reflection from the target (no multiple reflections), and that there is no dispersion or polarization changes due to the target.

The image-reconstruction algorithm derived in this section is a combination of the holographic (backward-wave) image reconstruction with a SAR image-reconstruction algorithm developed by Soumekh [12]–[14]. SAR imaging systems make use of wide-bandwidth data collected over a long linear aperture to form a cross-range by range 2-D image of terrain [27]. Inverse synthetic aperture imaging is similar, but utilizes angular diversity in favor of a linear scan [28]. Soumekh derived a wide-band SAR imaging algorithm that reconstructs data from a linear aperture into a 2-D image. The derivation presented in this section extends Soumekh's derivation by making the aperture planar instead of linear, which allows for a fully 3-D image reconstruction. The notation used is consistent with that used by Soumekh [12]–[14]. Slowly varying amplitude functions are typically ignored in the derivation, as they will not have a significant effect on the reconstructed image. Proper handling of the phase determines the effectiveness of the image reconstruction.

The wide-band reconstruction algorithm can be considered to be an extension of the single-frequency "backward-wave" holographic reconstruction algorithm to 3-D imaging by adding the

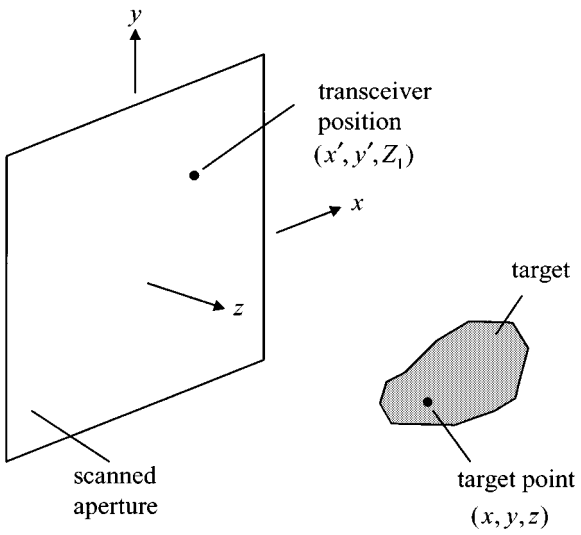

Fig. 2. Wide-band holographic-imaging system configuration.

range dimension to form 3-D wide-band holography. Equivalently, the algorithm could be referred to as a 3-D extension of SAR imaging to form a 3-D SAR.

A. Wide-Band Image-Reconstruction Algorithm

Data collection is performed by scanning a transmitting source and receiver over a rectilinear planar aperture that has one or more targets within its field of view. This system is quasi-monostatic, which means the transmitting and receiving antennas are separate, but in approximately the same location, and may be assumed to be coincident at the midpoint between the two antennas.

The measurement configuration is shown in Fig. 2, where the primed coordinates represent the position of the transceiver, and the unprimed coordinates represent a single point in the target or image space. If the target is characterized by a reflectivity function, i.e., $f(x,y,z)$, then the response measured by the transceiver will be the superposition of the reflectivity function times the roundtrip phase to the target. The measurement plane is at $z = Z_1$. The roundtrip phase is

$$2k\sqrt{(x-x')^2+(y-y')^2+(z-Z_1)^2} \tag{12}$$

where $k = \omega/c$ is the wavenumber, ω is the temporal angular frequency, and c is the speed of light.

The response measured at the transceiver is

$$s(x',y',\omega) = \iiint f(x,y,z) \times e^{-j2k\sqrt{(x-x')^2+(y-y')^2+(z-Z_1)^2}}\,dx\,dy\,dz. \tag{13}$$

The amplitude decay with range is not considered since it will have little impact on focusing the image. Alternatively, the data could be collected in the time domain, as is common with acoustic data. In this case, the data in (13) will be obtained by Fourier transforming the gathered data $s_t(x',y',t)$, which is the echoed data in the time domain

$$s(x',y',\omega) = \mathrm{FT}_{(t)}\left[s_t(x',y',t)\right] \tag{14}$$

where $\mathrm{FT}_{(t)}$ indicates Fourier transformation with respect to time.

The exponential term in (13) represents a spherical wave, which can be decomposed into an infinite superposition of plane waves

$$e^{-j2k\sqrt{(x-x')^2+(y-y')^2+(z-Z_1)^2}} = \iint e^{-jk_{x'}(x-x')-jk_{y'}(y-y')-jk_z(z-Z_1)}\,dk_{x'}\,dk_{y'} \tag{15}$$

where $k_{x'}$ and $k_{y'}$ are the Fourier-transform variables corresponding to x' and y', respectively. The spatial wavenumbers $k_{x'}$ and $k_{y'}$ will range from $-2k$ to $2k$ for propagating waves.

Using this decomposition into plane waves and rearranging yields

$$s(x',y',\omega) = \iint \underbrace{\left[\iiint f(x,y,z)e^{-j(k_{x'}x+k_{y'}y+k_zz)}\,dx\,dy\,dz\right]}_{F(k_{x'},k_{y'},k_z)} \times e^{jk_zZ_1}e^{jk_{x'}x'}e^{jk_{y'}y'}\,dk_{x'}\,dk_{y'} \tag{16}$$

where the triple integral in (16) represents a 3-D Fourier transform of the reflectivity function. The one-dimensional (1-D), 2-D, and 3-D Fourier transforms and their inverses are listed in the Appendix. Using this Fourier-transform relation gives

$$s(x',y',\omega) = \iint F(k_{x'},k_{y'},k_z)e^{jk_zZ_1}e^{j(k_{x'}x'+k_{y'}y')}\,dk_{x'}\,dk_{y'} = \mathrm{FT}_{2D}^{-1}\left\{F(k_{x'},k_{y'},k_z)e^{jk_zZ_1}\right\} \tag{17}$$

where FT indicates the Fourier transformation.

Taking the 2-D Fourier transform of both sides and dropping the distinction between the primed and unprimed coordinate systems yields

$$\mathrm{FT}_{2D}\{s(x,y,\omega)\} \equiv S(k_x,k_y,\omega) = F(k_x,k_y,k_z)e^{jk_zZ_1}. \tag{18}$$

To utilize this relationship in the reconstruction of the target image, the frequency ω needs to be expressed as a function of k_z. This is accomplished using the dispersion relation for plane waves in free-space or a uniform dielectric

$$k_x^2+k_y^2+k_z^2 = (2k)^2 = 4\left(\frac{\omega}{c}\right)^2. \tag{19}$$

Using this relation and inverting (18) yields

$$f(x,y,z) = \mathrm{FT}_{3D}^{-1}\{F(k_x,k_y,k_z)\} \tag{20}$$

where

$$F(k_x,k_y,k_z) = S(k_x,k_y,\omega)e^{-jk_zZ_1} \tag{21}$$

and

$$k_z = \sqrt{4k^2-k_x^2-k_y^2} = \sqrt{4(\omega/c)^2-k_x^2-k_y^2}. \tag{22}$$

Combining the above relations, results in the image reconstruction

$$f(x,y,z) = \mathrm{FT}_{3D}^{-1}\left\{\mathrm{FT}_{2D}\{s(x,y,\omega)\}e^{-j\sqrt{4k^2-k_x^2-k_y^2}Z_1}\right\}. \tag{23}$$

Equation (23) suffices for the reconstruction of the image if the data are defined continuously in x, y, and ω. However, for practical imaging configurations, the data will be discretely sampled at uniform intervals of position and frequency. Therefore, the data $s(x, y, \omega)$ are assumed to be uniformly sampled in each variable. Since the data are uniformly sampled in x and y, the 2-D FFT may be used to obtain a sampled version of $S(k_x, k_y, \omega)$. Since the angular frequency ω is a function of k_x, k_y and k_z, these data will contain samples of $F(k_x, k_y, k_z)$. However, these samples are nonuniformly spaced in k_z. The samples will be uniformly spaced in k_x and k_y, and will lie on concentric spheres of radius $2k$. In order to perform the inverse 3-D FFT in (20), the data will need to be resampled to uniformly spaced positions in k_z. This is easily accomplished using linear interpolation techniques.

B. Spatial and Frequency Sampling

Data gathering and image reconstruction will require that the data and the subsequent image be discretized. Successful discretization requires that the Nyquist sampling criterion be satisfied.

The sampling needed along the aperture is determined by a number of factors including the wavelength, size of the aperture, size of the target, and distance to the target. The Nyquist criterion will be satisfied if the phase shift from one sample point to the next is less than π rad. The worst case will occur for a target very near to the aperture and the sample points near the edge of the aperture. For a spatial sample interval of Δx, the worst case will have a phase shift of not more than $2k\Delta x$. Therefore, the sampling criterion can be expressed as

$$\Delta x < \frac{\lambda}{4} \tag{24}$$

where $\lambda = 2\pi/k$ is the wavelength.

This result is more restrictive than is usually required since the target is often a moderate distance from the aperture and the antenna beamwidth is usually less than 180°. For this reason, practical imaging systems can often employ sampling intervals on the order of $\lambda/2$.

The required frequency sampling is determined in a similar way. The phase shift resulting from a change in wavenumber Δk is $2\Delta k R_{\max}$, where $R_{\max}$ is the maximum target range. Requiring that this phase shift be less than π rad yields $\Delta k < \pi/2R_{\max}$ or

$$\Delta f < \frac{c}{4R_{\max}} \tag{25}$$

where Δf is the required frequency sampling interval.

Alternatively, the number of frequency samples for a bandwidth B must be

$$N_f > \frac{2R_{\max}}{(c/2B)}. \tag{26}$$

This is an interesting result since it indicates that two frequency samples are needed per range resolution cell, where the range resolution is defined by $c/2B$, as discussed in the following section.

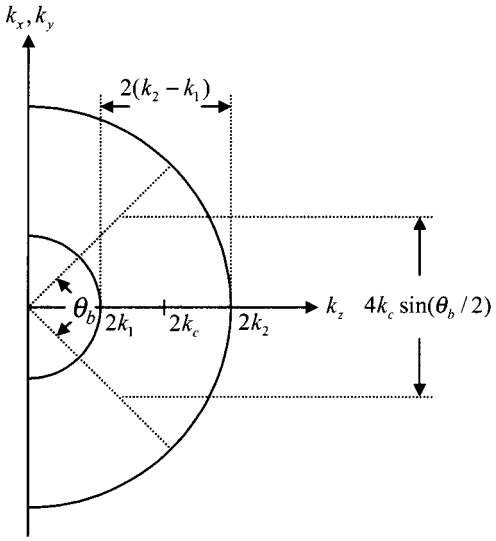

Fig. 3. Spatial frequency coverage in the range and cross-range directions.

C. Range and Cross-Range Resolution

The image-reconstruction technique discussed in the above sections relies on formation of the image in the spatial frequency domain. The resolution obtained in the image can be determined by examining the extent or width of the coverage in the spatial frequency domain. In one dimension, uniform frequency coverage (rect function) of width Δk results in a spatial pulsewidth of $\delta \approx 2\pi/\Delta k$. For the 3-D image reconstruction, the spatial frequency coverage is of the polar region shown in Fig. 3. If this region is approximated as rectangular, then the width in the k_x-direction is approximately $4k_c \sin(\theta_b/2)$, where k_c is the wavenumber at the center frequency and θ_b is the lesser of the full beamwidth of the antenna or the angle subtended by the aperture. This results in a cross-range resolution of

$$\delta_x \approx \frac{\lambda_c}{4\sin(\theta_b/2)}. \tag{27}$$

For an aperture-limited system with range R much greater than the aperture D, the cross-range resolution may be approximated by

$$\delta_x \approx \frac{\lambda_c}{2} F\# \tag{28}$$

where $F\# \equiv R/D$ is the optical F number.

Cross-range resolution in the y-direction will be the same, except that the F number or beamwidth may be different.

The spatial frequency width in the k_z direction is $2(k_2 - k_1)$, where k_1 and k_2 are the wavenumbers at the low and high frequencies of the system. This width results in a range resolution of approximately

$$\delta_z \approx \frac{2\pi}{2(k_2 - k_1)} = \frac{c}{2B} \tag{29}$$

where B is the temporal frequency bandwidth of the system.

IV. Laboratory Scanned Imaging Results

A laboratory x–y scanner coupled with various single frequency and wide-band transceivers have been used to gather

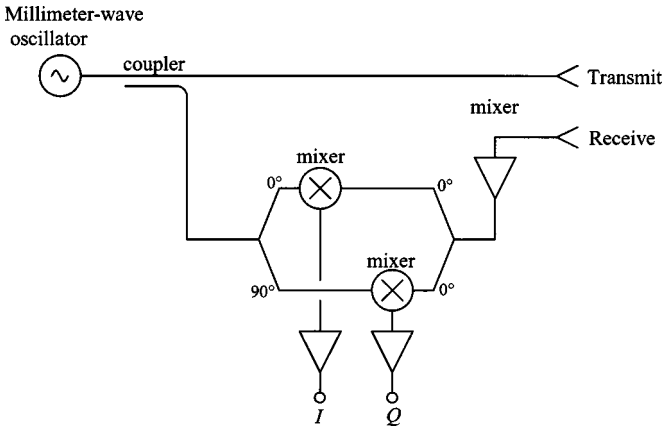

Fig. 4. Simplified holographic transceiver.

data to test the efficacy of the algorithms described in Section III.

A. Single-Frequency Imaging Results

A simplified schematic for a single-frequency microwave transceiver is shown in Fig. 4. In this transceiver, the millimeter-wave signal is generated using a millimeter-wave oscillator, typically a Gunn diode oscillator. The transmitted signal is launched using a small wide-beamwidth antenna, often a small pyramidal waveguide horn. The transmitted signal is reflected from the target, and then received by the receive antenna. The receive antenna is usually of the same size and type as the transmit antenna and is placed immediately adjacent to the transmit antenna. In this way, the pair of antennas simulates a single antenna, but with significantly higher transmit to receive isolation. The received signal is then mixed with in-phase (0° phase shift) and quadrature (90° phase shift) signals coupled from the millimeter-wave oscillator. The resulting signals are called I and Q for in-phase and quadrature, and contain the complex scattered waves amplitude and phase

$$I + jQ = Ae^{-j2kR} \tag{30}$$

where A is the amplitude of the scattered signal, R is the distance to the target, and k is the wavenumber. This signal is sampled over an x–y aperture using a 2-D x–y scanner to obtain the input to the image-reconstruction algorithm $s(x, y, \omega)$ (Note: $k = \omega/c$, where c is the speed of light).

A single-frequency 35-GHz transceiver was used to generate an image of a clothed mannequin with a large concealed metal pellet gun. The results are shown in Fig. 5. The hologram image shows the raw data, which are input to the image-reconstruction algorithm. Only the real-part (I) is shown, the quadrature signal (Q) is phase shifted by 90° and is qualitatively similar. The reconstructed image shows resolution on the order of 5 mm, and the handgun is easily recognized in the image. The image of the body of the mannequin shows the effects of speckle. Speckle is due to complex interference from varying reflection points on the body at different ranges. This effect is largely eliminated using the wide-band 3-D imaging technique discussed in Section III.

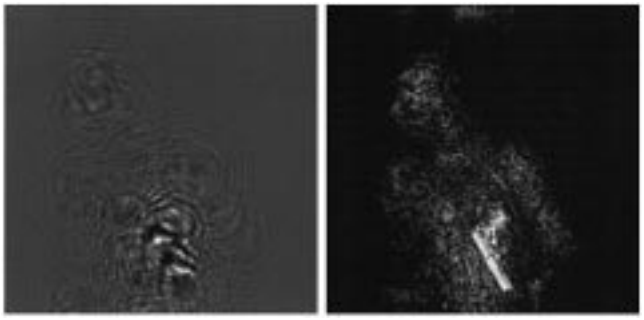

(a) (b)

Fig. 5. (a) 35-GHz hologram and (b) reconstructed image of a mannequin carrying a concealed handgun.

Fig. 6. 350-GHz reconstructed image of a Glock-17 9-mm handgun.

A 350-GHz transceiver has been used to demonstrate the level of resolution that is ultimately achievable with millimeter-wave holography. A reconstructed 350-GHz image of a Glock-17 is shown in Fig. 6. In the image, the aperture is 25 cm × 25 cm, and the depth to the target is 7.4 cm. The hologram consisted of 512 × 512 data points, sampled at approximately 0.5-mm intervals. The scan required approximately 10 min to complete. This image shows a resolution size of less than 1 mm. Due to the very large number of samples required at this frequency, a practical weapon detection system is expected to operate at a frequency of 100 GHz or lower.

B. Wide-Band Imaging Results

More complex targets, such as a person carrying concealed weapons, will have a significant depth of field. A high-resolution (low F number) imaging system will have a very sharp depth of focus, and will be unable to focus all areas in the image simultaneously. For this reason, the 3-D wide-band imaging technique was developed.

A wide-band holographic transceiver operates in the same manner as the single-frequency transceiver shown in Fig. 4, except that the frequency is repeatedly swept over the frequency range of interest. A voltage-controlled oscillator (VCO) is typically used as the millimeter-wave oscillator to allow frequency sweeping. The I and Q signals will be waveforms, which must be sampled according to the criteria established in Section III-C.

In Fig. 7, a 100–112-GHz wide-band holographic image of a Glock-17 is shown. This image has a resolution of better than 3 mm. The trigger guard and parts of the handle of the Glock are

(a) (b)

Fig. 7. (a) Optical image and (b) 100–112-GHz wide-band holographic image of a Glock-17 handgun.

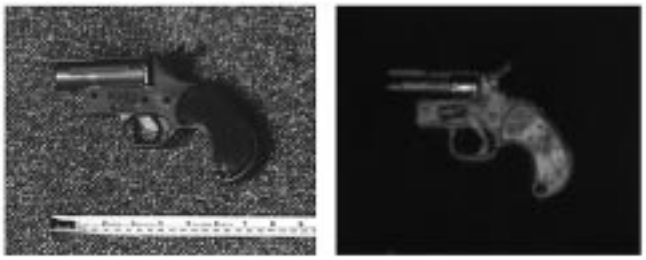

(a) (b)

Fig. 8. (a) Optical image and (b) 100–112-GHz wide-band holographic image of an Olin plastic flare gun.

made from plastic. These components show up in the image, but as expected, are at somewhat lower intensity. A plastic Olin flare gun was imaged, with the results shown in Fig. 8. This gun is entirely plastic, except for a small piece of metal near the start of the barrel. This metal component is clearly brighter in the image. The scans in Figs. 7 and 8 used an aperture of approximately 30 cm $\times$ 30 cm with a discretization of 256 (x) $\times$ 256 (y) $\times$ 128 (f), and required approximately 20 min to scan. Fig. 9 shows optical and millimeter-wave (100–112 GHz) images of a mannequin with a concealed weapon. This image demonstrates the resolution that is achievable with millimeter-wave imaging. Fine details are apparent in the millimeter-wave image including the embroidery (Massachusetts Institute of Technology (MIT) logo) and the duct tape used to hold the weapon on the mannequin. The scan in Fig. 9 used an aperture of approximately 80 cm $\times$ 140 cm with a discretization of 512 (x) $\times$ 1024 (y) $\times$ 128 (f), and required approximately 3 h to scan. The scan time is limited by the relatively slow sweeping YIG-based oscillators in the laboratory transceiver that was used.

V. Real-Time Wide-Band Holographic Imaging System

A practical implementation of wide-band holographic imaging requires a full-body scan in about 1–2 s (or less). A full-body scan requires sampling at less than one-wavelength spacing over an aperture of at least 0.70 m $\times$ 2.0 m. Scanning a single transmitter receiver (transceiver) over this aperture requires at least several minutes. Therefore, to scan the target in a reasonable time requires an electronically switched array of antennas. A 2-D array of antennas would be ideal since it would not require any moving parts and could, therefore, operate at video frame rates (10–30 frames/s). The cost and complexity of a large 2-D high-resolution array renders it impractical at this

(a) (b)

Fig. 9. (a) Optical image and (b) 100–112 GHz wide-band holographic image of a clothed mannequin with a concealed Glock-17 handgun.

Fig. 10. Current wide-band holographic millimeter-wave imaging system.

time. A linear array can, however, be fabricated for reasonable cost, and can be scanned quickly to gather full-aperture image data.

The wide-band imaging system has been developed that utilizes a scanned linear array of antennas to quickly gather the image data for subsequent reconstruction and display [11], [29]–[31]. A photograph of this system is shown in Fig. 10. A block diagram of the system is shown in Fig. 11. The system consists of a sequentially switched linear array of antennas driven by a wide-band millimeter-wave transceiver. The array and transceiver are mounted on a large fast mechanical scanner, which allows a full image data set to be gathered in less than 1 s. During a scan, the array is sequenced electronically at very high speed to gather each line of data as the scanner is moving down, thereby gathering a full 2-D aperture of data.

This system operates in the Ka-frequency band (26.5–40 GHz) with the current system configured to operate from 27 to 33 GHz. There are 128 antenna elements organized as an upper row of 64 transmit antennas, and a lower row of 64 receive antennas. Logic circuitry sequences the transmit and receive antennas to transmit from one antenna and receive the wide-band signal from each of the two neighboring antennas in the receive row. This places a virtual sampling point halfway in between each transmit and receive antenna. The transmit row and receive row are offset by half the antenna

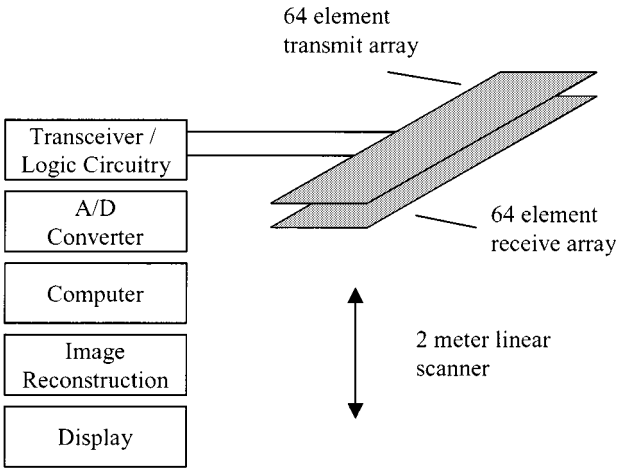

Fig. 11. Block diagram of imaging system.

spacing, thus, the effective sample spacing is one-half of the single-row antenna spacing. This sequencing scheme cannot be used on the last antenna element, thus, the effective number of sample points is 127. The horizontal aperture width is 72.6 cm, which yields an effective sample spacing of 5.7 mm.

The wide-band data are sampled horizontally across the array and vertically over the aperture, and are digitized by an A/D converter for subsequent storage in the computer. After digitizing, the reconstruction algorithm discussed in Section III is applied to reconstruct the 3-D image of the target. The 3-D image is then collapsed using a maximum value projection into a fully-focused 2-D image of the target for display on the computer.

A photograph of the wide-band array is shown in Fig. 12. The transmit row switched antenna array is composed of eight single-pole eight-throw (SP8T) p-i-n-diode waveguide switches, interconnected with a waveguide manifold feed and fed by a ninth SP8T waveguide switch. Each of the 64 outputs has a small dielectric polyrod antenna inserted into the waveguide. The polyrods can be of any length, however, the ones used here are four wavelengths long (at 35 GHz). The receive-row switched antenna array is identical and is placed back to back with the transmit array. Integrated switch drivers are contained within each SP8T switch module, allowing a simple connector with power and coded logic inputs to each of the 18 SP8T switch modules.

A simplified schematic diagram of the transceiver is shown in Fig. 13. The RF VCO is swept from 27 to 33 GHz. This transceiver is a heterodyne design with the heterodyne offset frequency obtained by offsetting the local oscillator (LO) by an IF (in this case, 600 MHz). An IF reference signal (at 600 MHz) is obtained by mixing coupled signals from the RF and LO oscillators. The phase and amplitude of the scattered signal are contained within the IF receive signal, which is the received signal down converted using the LO oscillator. The in-phase (I) and quadrature (Q) signals are obtained by mixing the two signals with and without a 90° phase shift, as shown in the figure. The I and Q signals contain the complex scattered wave's amplitude and phase $I + jQ = Ae^{-j2kR}$, where A is the amplitude of the scattered wave and R is the range to the target. This signal is sampled over the frequency range of the system

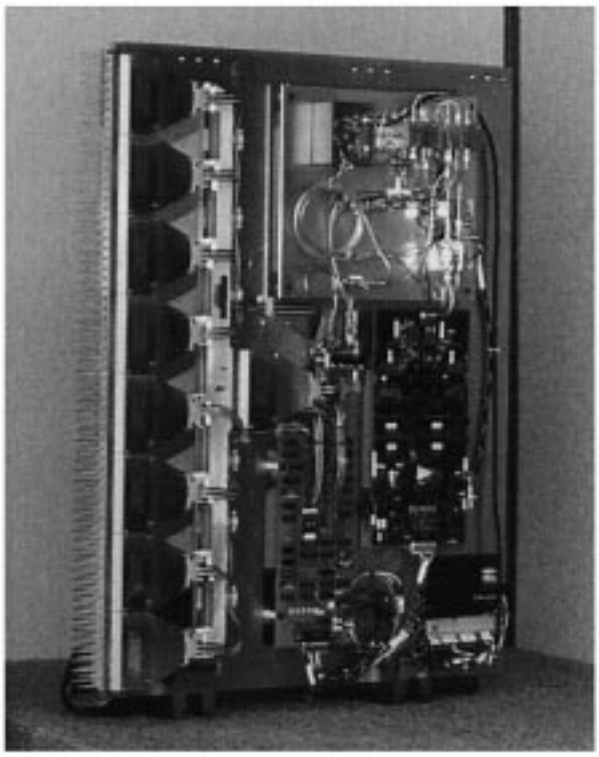

Fig. 12. Photograph of the linear array.

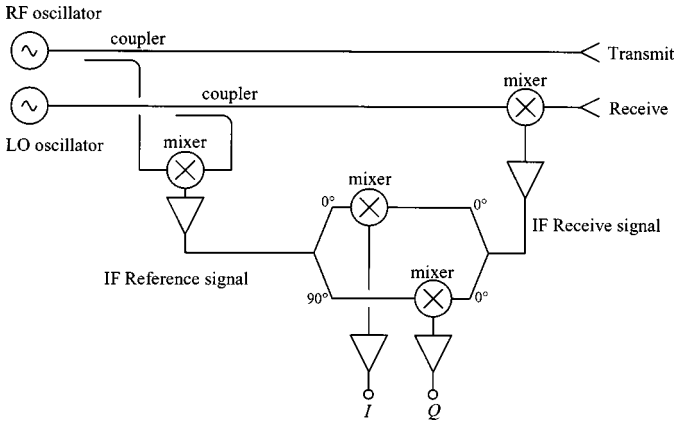

Fig. 13. Simplified schematic of a millimeter-wave transceiver.

(27–33 GHz) and sampled over an x–y aperture using the sequentially switched linear array and vertical scanner to obtain the input to the image-reconstruction algorithm $s(x, y, \omega)$.

The data are discretely sampled with typical dimensions of 127 x samples, 512 y samples, and 64 frequency samples with spatial and frequency steps sizes of 5.7 mm (x), 3.9 mm (y), and 94 MHz (f), respectively. The frequency sweep time is 20 μs and the integration time per frequency is 0.3 μs. The IF bandwidth is approximately 2.5 MHz. The image-reconstruction time is very dependent on the type of computer system used to perform the image reconstruction. The Unix-based SUN computers (approximately 1995) require several minutes to perform the reconstruction. A dedicated multiprocessor digital signal processor (DSP) (Analog Devices SHARC-based, 1998) requires less than 10 s to perform the reconstruction.

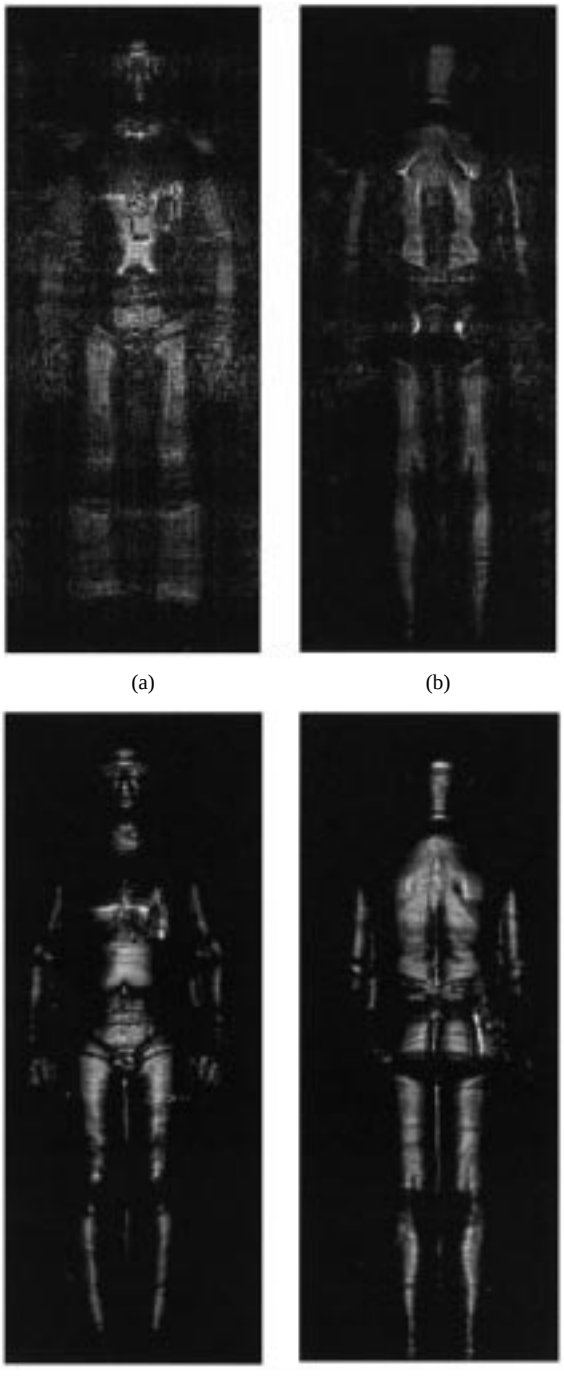

(a) (b)

(c) (d)

Fig. 14. (a), (b) Single-frequency (35 GHz) images of a man. (c), (d) Wide-band (27–33 GHz) images of the same man.

After the sampled data have been recorded by the A/D converter, a Unix-based SUN computer workstation then performs the image reconstruction.

VI. Real-Time Imaging Results

The wide-band millimeter-wave imaging system described in the previous section has been tested extensively on personnel carrying concealed weapons. In all cases, the data were gathered in near real-time (approximately 1 s). Fig. 14 shows the dramatic improvement in image quality that has been obtained by converting the single-frequency millimeter-wave imaging system to wide-band operation. The single-frequency images show significant degradation due to lack of focus over many parts of the image. In addition, some degradation is apparent due to poor sensitivity in the single-frequency transceiver. By contrast, the wide-band images are fully focused due to the 3-D image reconstruction. Significantly higher dynamic range is also apparent in the wide-band images. This is due to better focus, as well as the high sensitivity, of the transceiver design.

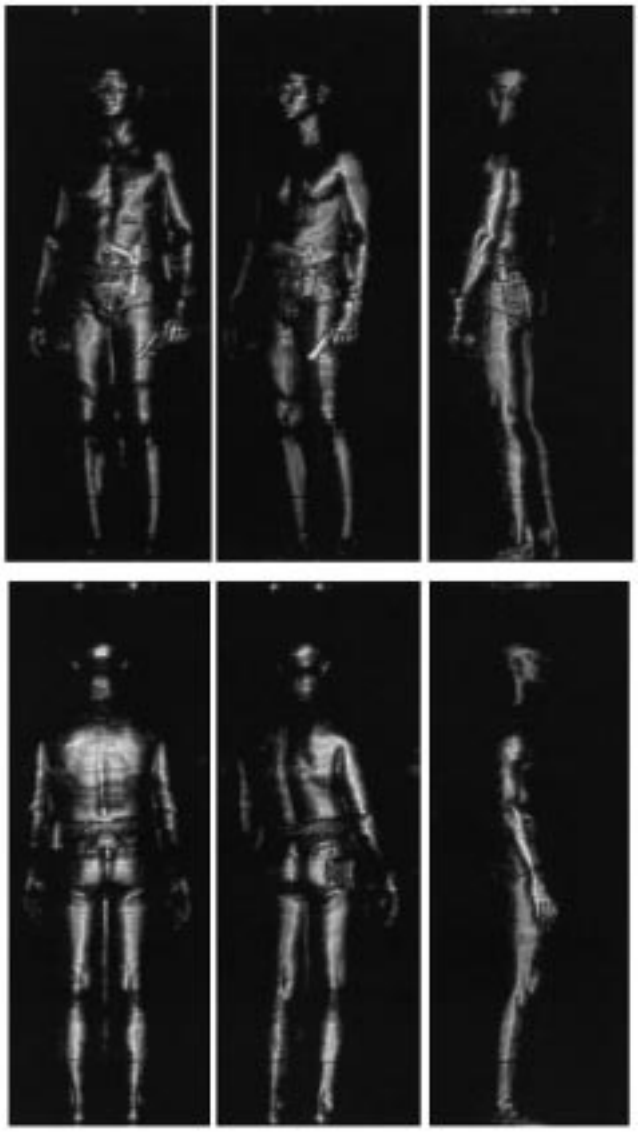

Fig. 15. Wide-band images of a man carrying concealed handguns along with innocuous items.

Fig. 15 shows six wide-band (27–33 GHz) images of a man carrying two concealed handguns, as well as several innocuous items. The first image shows a Glock-17 handgun tucked at the beltline under the man's shirt. The second image shows a small handgun in the man's left-hand-side pants pocket. The third image shows a vinyl/paper checkbook in the left-hand-side back pocket. The fifth image shows a leather wallet in the man's right-hand-side back pocket.

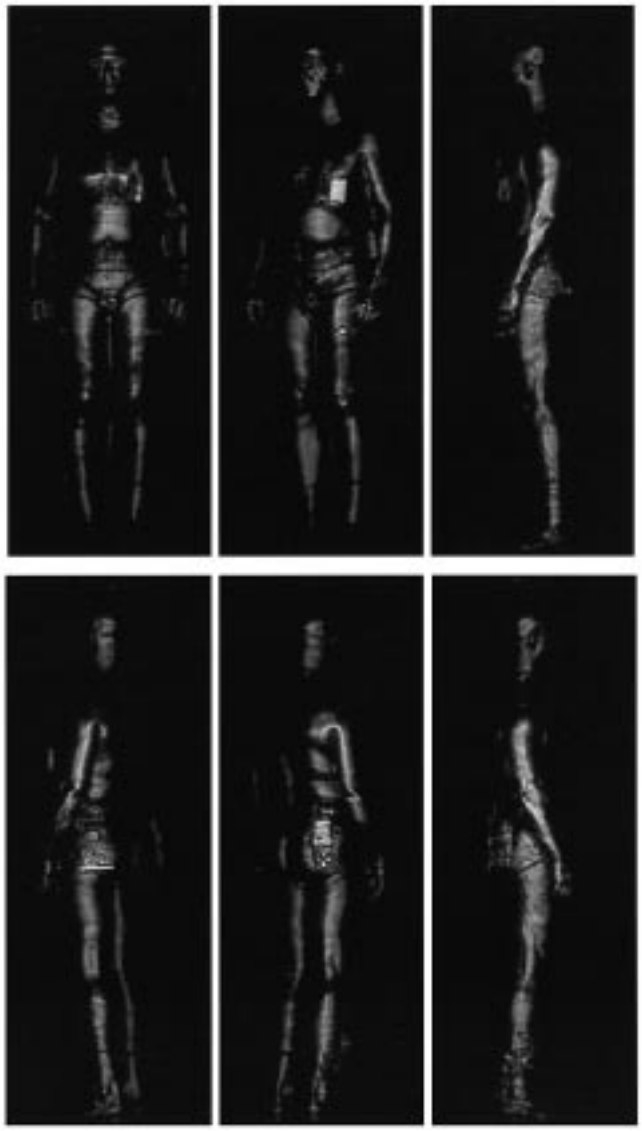

Fig. 16. Wide-band images of a man carrying two handguns along with innocuous items.

Fig. 16 shows a similar set of images of a different man carrying two concealed weapons, as well as several innocuous items. The first image shows a typical front view. The second image shows a concealed pack of cigarettes in the man's left-hand-side shirt pocket and keys in the left-hand-side front pants pocket. The fourth image shows a small handgun concealed in the left-hand-side back pants pocket. The fifth image shows a "walkie-talkie"-style radio in the right-hand-side back pocket. Comparison of the third and sixth images allows discernment of a concealed object on the lower right leg (in the sixth image). This item is an Olin plastic flare gun, which is used to demonstrate the plastic detection capability of the wide-band millimeter-wave imaging system.

Fig. 17 shows an optical image of a man with a block of plastic explosive royal demolition explosive (RDX) concealed on his back. Also shown are millimeter-wave images (27–33 GHz) of the man with and without the concealed explosive. The explosive is subtly, but clearly, visible along the man's spine.

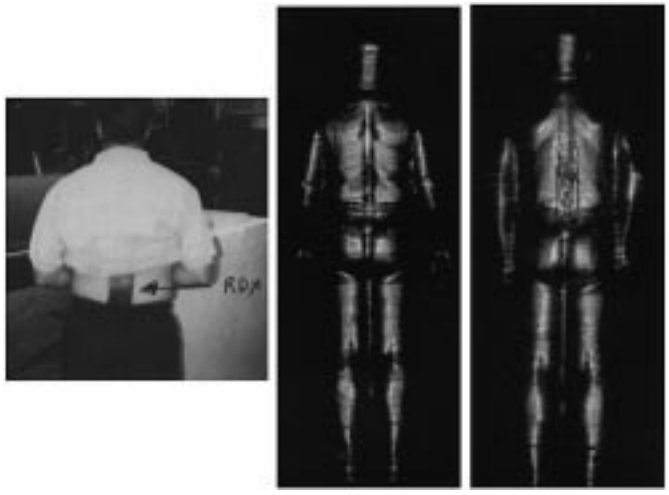

(a) (b) (c)

Fig. 17. (a) Optical image showing the location and orientation of a concealed RDX plastic explosive. 27–33-GHz millimeter-wave images of a man: (b) without and (c) with the concealed explosive.

VII. Conclusion

This paper has demonstrated the techniques developed for PNNL's wide-band millimeter-wave holographic surveillance system. This system uses coherent wide-band millimeter-wave illumination to form 3-D fully focused images for personnel surveillance applications. The 3-D image-reconstruction algorithm developed for this system uses no far-field assumptions, and has near theoretically optimal resolution performance in all three dimensions. The wide-band imaging technique largely eliminates the effects of speckle, which are prevalent in single-frequency coherent imaging techniques. In addition, the near-field wide-angle scanned-source configuration produces excellent illumination properties. The surface of the target is illuminated over a wide angular extent, both horizontally and vertically. This reduces the effects of shadowing due to specular reflection.

Numerous laboratory-imaging results have been shown to demonstrate the high-resolution and image fidelity that are achievable using this millimeter-wave imaging technique. A high-speed imaging system prototype has been developed to implement this imaging technique in near real time. Imaging results obtained using actual personnel have been shown to demonstrate the effectiveness of this system for the detection and identification of concealed objects, including innocuous items, plastic and metal weapons, and plastic explosives. Other contraband items such as drugs, large amounts of money, etc. could also be detected with this type of system.

Appendix
Fourier-Transform Definitions

Fourier transforms are useful for converting a function between time and frequency domains, but also for converting between space- and spatial-frequency domains. Both spatial and temporal Fourier transforms are common in wide-band imaging. Typically, the time or space function will be denoted with a lower case letter, whereas the frequency-domain function will

use a capital letter. All versions of the Fourier-transform operator will often be denoted by FT. The inverse Fourier transform operator will often be denoted by FT^{-1}. A function f and its Fourier transform F are considered to be a Fourier-transform pair denoted by

$$f \Leftrightarrow F. \tag{A1}$$

The temporal Fourier transform and its inverse are defined by

$$F(\omega) = \int f(t) e^{-j\omega t}\, dt = \mathrm{FT}\{f(t)\} \tag{A2}$$

$$f(t) = \frac{1}{2\pi} \int F(\omega) e^{j\omega t}\, d\omega = \mathrm{FT}^{-1}\{F(\omega)\}. \tag{A3}$$

The 1-D spatial Fourier transform and its inverse are defined by

$$F(k_x) = \int f(x) e^{-jk_x x}\, dx = \mathrm{FT}_{1D}\{f(x)\} \tag{A4}$$

$$f(x) = \frac{1}{2\pi} \int F(k_x) e^{jk_x x}\, dk_x = \mathrm{FT}_{1D}^{-1}\{F(k_x)\}. \tag{A5}$$

The 2-D spatial Fourier transform and its inverse are defined by

$$\begin{aligned} F(k_x, k_y) &= \iint f(x,y) e^{-j(k_x x + k_y y)}\, dx\, dy \\ &= \mathrm{FT}_{2D}\{f(x,y)\} \end{aligned} \tag{A6}$$

$$\begin{aligned} f(x,y) &= \frac{1}{(2\pi)^2} \iint F(k_x, k_y) e^{j(k_x x + k_y y)}\, dk_x\, dk_y \\ &= \mathrm{FT}_{2D}^{-1}\{F(k_x, k_y)\}. \end{aligned} \tag{A7}$$

The 3-D spatial Fourier transform and its inverse are defined by

$$\begin{aligned} F(k_x, k_y, k_z) &= \iiint f(x,y,z) e^{-j(k_x x + k_y y + k_z z)}\, dx\, dy\, dz \\ &= \mathrm{FT}_{3D}\{f(x,y,z)\} \end{aligned} \tag{A8}$$

$$\begin{aligned} f(x,y,z) &= \frac{1}{(2\pi)^3} \iiint F(k_x, k_y, k_z) \\ &\quad \times e^{j(k_x x + k_y y + k_z z)}\, dk_x\, dk_y\, dk_z \\ &= \mathrm{FT}_{3D}^{-1}\{F(k_x, k_y, k_z)\}. \end{aligned} \tag{A9}$$

REFERENCES

[1] H. D. Collins, D. L. McMakin, T. E. Hall, and R. P. Gribble, "Real-time holographic surveillance system," U.S. Patent 5 455 590, Oct. 3, 1995.

[2] G. R. Huguenin, P. F. Goldsmith, N. C. Deo, and D. K. Walker, "Contraband Detection System," U.S. Patent 5 073 782, Dec. 17, 1991.

[3] G. R. Huguenin, "A millimeter wave focal plane array imager," *Proc. SPIE—Int. Soc. Opt. Eng.*, vol. 2211, pp. 300–301, 1994.

[4] N. H. Farhat, "Microwave holography and its applications in modern aviation," in *Proc. SPIE Eng. Applicat. Holography Symp.*, 1972, pp. 295–314.

[5] G. Tricoles and N. H. Farhat, "Microwave holography: Applications and techniques," *Proc. IEEE*, vol. 65, pp. 108–121, Jan. 1977.

[6] B. P. Hildebrand and K. A. Haines, "Holography by scanning," *J. Opt. Soc. Amer.*, vol. 59, pp. 1–6, 1969.

[7] B. P. Hildebrand and B. B. Brenden, *An Introduction to Acoustical Holography*. New York: Plenum, 1972.

[8] D. Gabor, "A new microscope principle," *Nature*, vol. 161, 1948.

[9] E. N. Leith and J. Upatnieks, "Reconstructed wavefronts and communication theory," *J. Opt. Soc. Amer.*, vol. 52, pp. 1123–1130, 1962.

[10] N. H. Farhat and W. R. Guard, "Millimeter wave holographic imaging of concealed weapons," *Proc. IEEE*, vol. 59, pp. 1383–1384, Sept. 1971.

[11] D. M. Sheen, H. D. Collins, T. E. Hall, D. L. McMakin, R. P. Gribble, R. H. Severtsen, J. M. Prince, and L. D. Reid, "Real-time wideband holographic surveillance system," U.S. Patent 5 557 283, Sept. 17, 1996.

[12] M. Soumekh, "Bistatic synthetic aperture radar inversion with application in dynamic object imaging," *IEEE Trans. Signal Processing*, vol. 39, pp. 2044–2055, Sept. 1991.

[13] ——, "A system model and inversion for synthetic aperture radar imaging," *IEEE Trans. Image Processing*, vol. 1, pp. 64–76, Jan. 1992.

[14] ——, *Fourier Array Imaging*. Englewood Cliffs, NJ: Prentice-Hall, 1994.

[15] T. H. Chu and N. H. Farhat, "Frequency-swept microwave imaging of dielectric objects," *IEEE Trans. Microwave Theory Tech.*, vol. 36, pp. 489–493, Mar. 1988.

[16] N. H. Farhat, C. L. Werner, and T. H. Chu, "Prospects for three-dimensional projective and tomographic imaging radar networks," *Radio Sci.*, vol. 19, pp. 1347–1355, 1984.

[17] D. C. Munson, J. D. O'Brien, and W. K. Jenkins, "A tomographic formulation of spotlight-mode synthetic aperture radar," *Proc. IEEE*, vol. 71, pp. 917–925, Aug. 1983.

[18] C. K. Chan and N. H. Farhat, "Frequency swept tomographic imaging of three-dimensional perfectly conducting objects," *IEEE Trans. Antennas Propagat.*, vol. AP-29, pp. 312–319, Feb. 1981.

[19] W.-M. Boerner, C.-M. Ho, and B.-Y. Foo, "Use of radon's projection theory in electromagnetic inverse scattering," *IEEE Trans. Antennas Propagat.*, vol. AP-29, pp. 336–341, Feb. 1981.

[20] Y. Das and W. M. Boerner, "On radar target shape estimation using algorithms for reconstruction from projections," *IEEE Trans. Antennas Propagat.*, vol. AP-26, pp. 274–279, Feb. 1978.

[21] N. H. Farhat, "Principles of broad-band coherent imaging," *J. Opt. Soc. Amer.*, vol. 67, pp. 1015–1021, 1977.

[22] S. R. Raz, "On scatterer reconstruction from far-field data," *IEEE Trans. Antennas Propagat.*, vol. AP-24, pp. 66–70, Jan. 1976.

[23] R. M. Lewis, "Physical optics inverse diffraction," *IEEE Trans. Antennas Propagat.*, vol. AP-17, pp. 308–314, Mar. 1969.

[24] N. Bojarski, "Inverse Scattering," U.S. Naval Air Command, Final Rep. N000 19-73-C-0312F, Feb. 1974.

[25] A. L. Boyer, "Reconstruction of ultrasonic images by backward propagation," in *Acoustic Holography*. New York: Plenum, 1970, vol. 3, pp. 333–384.

[26] J. W. Goodman, *Introduction to Fourier Optics*. New York: McGraw-Hill, 1968.

[27] D. A. Ausherman, A. Kozma, J. L. Walker, H. M. Jones, and E. C. Poggio, "Developments in radar imaging," *IEEE Trans. Aerosp. Electron. Syst.*, vol. AES-20, pp. 363–400, July 1984.

[28] J. L. Walker, "Range-Doppler imaging of rotating objects," *IEEE Trans. Aerosp. Electron. Syst.*, vol. AES-16, pp. 23–52, Jan. 1980.

[29] D. L. McMakin, D. M. Sheen, H. D. Collins, T. E. Hall, and R. R. Smith, "Millimeter-wave high resolution holographic surveillance system," in *Proc. SPIE Int. Substance Identification Technol. Symp.*, vol. 2092, 1993, pp. 525–535.

[30] D. L. McMakin, D. M. Sheen, H. D. Collins, T. E. Hall, and R. H. Severtsen, "Wideband, millimeter-wave, holographic weapons surveillance system," in *Proc. SPIE European Opt. Environmental Public Safety Symp.*, vol. 2511, 1995, pp. 131–141.

[31] D. M. Sheen, D. L. McMakin, H. D. Collins, T. E. Hall, and R. H. Severtsen, "Concealed explosive detection on personnel using a wideband holographic millimeter-wave imaging system," in *Proc. SPIE Aerosp./Defense Sens. Contr.*, vol. 2755, 1996, pp. 503–513.

David M. Sheen was born in Richland, WA. He received the B.S. degree in electrical engineering from Washington State University, Pullman, in 1985, and the M.S. and Ph.D. degrees in electrical engineering at the Massachusetts Institute of Technology, Cambridge, in 1988 and 1991, respectively.

He is currently a Staff Engineer at Battelle, Pacific Northwest National Laboratory (PNNL), Richland, WA. His research interests are in the areas of millimeter-wave and acoustic imaging, electromagnetics, optics, antennas, and signal/image processing. He is also an adjunct faculty member at Washington State University Tri-Cities, Richland, WA, where he is currently teaches courses in electromagnetic fields and waves.

Douglas L. McMakin was born in Richland, WA. He received the B.S. degree in electrical engineering degree from Washington State University, Pullman, in 1986.

Since October 1987, he has been with Battelle, Pacific Northwest National Laboratory (PNNL), Richland, WA, where he is currently a Staff Engineer. He has been involved in the development of innovative near real-time and microwave and millimeter-wave holographic-imaging systems. He has also performed numerous laboratory experiments using various radar imaging techniques such as SAR, focused lens, and holography using continuous wave, impulse, and sweep frequency transceivers in the 1–350-GHz frequency range.

Thomas E. Hall was born in Richland, WA, on September 27, 1952. He received the B.S. and M.S. degrees in electrical engineering from Washington State University, Pullman, in 1975 and 1977, respectively.

He is currently with Battelle, Pacific Northwest National Laboratory (PNNL), Richland, WA. He possesses over 20 years experience in numerical processing and analysis for ultrasonic and radar imaging systems. His research interests are in practical computer solutions to support 3-D real-time near-field radar imaging systems.